

Multi-Component VAE with Gaussian Markov Random Field

Fouad Oubari

*Université Paris-Saclay, CNRS, ENS Paris-Saclay,
Centre Borelli
Paris, France
oubarifouad@gmail.com*

Mohamed El Baha

*Manufacture Française des Pneumatiques Michelin
Clermont-Ferrand, France
elbahamohamed@gmail.com*

Raphael Meunier

*Manufacture Française des Pneumatiques Michelin
Clermont-Ferrand, France
raphael.meunier@michelin.com*

Rodrigue Décatoire

*Manufacture Française des Pneumatiques Michelin
Clermont-Ferrand, France
rodrigue.decatoire@michelin.com*

Mathilde Mougeot

*Université Paris-Saclay, CNRS, ENS Paris-Saclay, Centre Borelli
Gif-sur-Yvette, France
mathilde.mougeot@ens-paris-saclay.fr
ENSIE
Évry, France*

Abstract—Multi-component datasets with intricate dependencies, like industrial assemblies or multi-modal imaging, challenge current generative modeling techniques. Existing Multi-component Variational AutoEncoders typically rely on simplified aggregation strategies, neglecting critical nuances and consequently compromising structural coherence across generated components. To explicitly address this gap, we introduce the Gaussian Markov Random Field Multi-Component Variational AutoEncoder, a novel generative framework embedding Gaussian Markov Random Fields into both prior and posterior distributions. This design choice explicitly models cross-component relationships, enabling richer representation and faithful reproduction of complex interactions. Empirically, our GMRF MCVAE achieves state-of-the-art performance on a synthetic Copula dataset specifically constructed to evaluate intricate component relationships, demonstrates competitive results on the PolyMNIST benchmark, and significantly enhances structural coherence on the real-world BIKED dataset. Our results indicate that the GMRF MCVAE is especially suited for practical applications demanding robust and realistic modeling of multi-component coherence.

I. INTRODUCTION

Multi-component datasets, ranging from medical imaging (CT-MRI pairs) [1], [2] to finance (multiple correlated markets) [3], [4] and industrial design (structured assemblies) [5], [6] are prevalent in real-world applications. Generating such data requires models that capture both component-wise intricacies and cross-component interactions. For instance, in an indus-

trial setting, each component of a system must be generated in a way that preserves overall structural and functional coherence.

Although various generative approaches exist for multimodal data [7], [8], many rely on simplified aggregation schemes that overlook nuanced inter-component factors. Hence, we investigate Markov Random Fields (MRFs) as a structured way to encode the relationships more explicitly. By decomposing the latent distribution into terms that reflect how components relate to each other [9], MRFs allow more nuanced interactions to be embedded, potentially leading to generations that better preserve global consistency.

A. Contributions

To address the limitations of existing multi-component Variational AutoEncoders (MCVAEs), we propose the Gaussian Markov Random Field Multi-Component Variational AutoEncoder (GMRF MCVAE), which enhances cross-component modeling while maintaining tractable inference. Our main contributions are:

- **Gaussian MRF Multi-Component VAE.** We introduce a novel multi-component VAE architecture that embeds a Gaussian Markov Random Field (GMRF) in both the prior and posterior, enabling richer inter-component correlations than standard factorized or mixture-based methods.

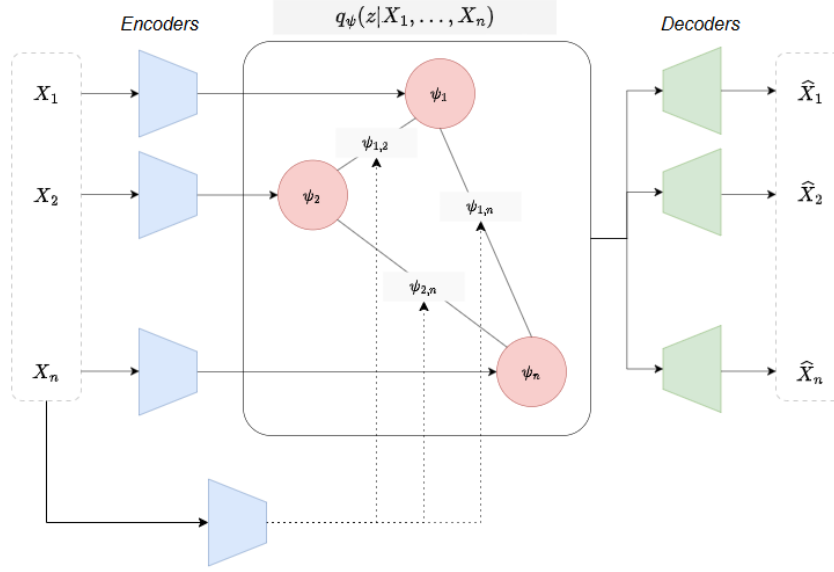


Fig. 1. A general MRF-based Multi-Component VAE: each component is assigned its own encoder-decoder pair, where the encoder learns unary potentials ψ_i . A global encoder models pairwise potentials $\psi_{i,j}$ among components. Sampling \mathbf{z} from this MRF-based latent space captures cross-component relationships. In practice, we adopt a Gaussian assumption for computational simplicity.

- **Practical Covariance Construction and Conditional Sampling.** We propose a blockwise covariance assembly that guarantees symmetric positive definiteness while capturing component-to-component interactions. Further, closed-form Gaussian conditioning enables efficient conditional generation without additional training.
- **Robust Empirical Validation.** Our GMRF MCVAE achieves state-of-the-art performance on a synthetic Copula dataset designed to test intricate cross-component structure, shows competitive results on the PolyMNIST benchmark with more complex components, and outperforms baselines on the real-world BIKED dataset in both perceptual quality and structural coherence.

To position our work within the broader landscape of generative modeling, we next review relevant literature on multi-component VAEs and Markov Random Fields, highlighting both their strengths and limitations.

II. RELATED WORK

A. Multi-Component VAEs

The field of multi-component generative models has seen substantial growth recently. Within this domain, VAE-based models have distinguished themselves due to their rapid and tractable sampling capabilities [10], as well as their robust generalization performance [11]. The essence of multi-component generation lies in its ability to learn a joint latent representation from multiple data components, encapsulating a unified distribution. Traditional MCVAE frameworks typically adopt a structure with separate encoder/decoder pairs for each component, coupled with an aggregation mechanism to encode a cohesive joint representation across all components.

A variety of methodologies have been introduced to synthesize these distributions within the latent space.

A seminal approach by [7] suggests that the joint latent posterior can be effectively approximated through using the Product of Experts (PoE) assumption. This strategy facilitates the generation of cross components at inference time without requiring an additional inference network or a multistage training process, marking a significant advancement over previous methodologies [12], [13]. However, this approach implicitly relies on the assumption that the posterior distribution can be approximated by factorizing distributions. This assumption presupposes independence among components, which may not be true. This assumption overlooks the complex inter-component relationships intrinsic to the data, potentially limiting the model’s ability to fully capture the richness of multi-component interactions.

An alternative framework proposed by [8] employs a Mixture of Experts (MoE) strategy for aggregating marginal posteriors. This method stands in contrast to the approach used in the MVAE [7], which, according to the authors, is susceptible to a ‘veto phenomenon’ a scenario where an exceedingly low marginal posterior density significantly diminishes the joint posterior density. In contrast, the MoE paradigm mitigates the risk associated with overly confident experts by adopting a voting mechanism among experts, thereby distributing its density among all contributing experts. However, a critique by [14] highlights a fundamental limitation of the MMVAE approach: it tends to average the contribution of each component. Given that the model employs each component-specific encoder to reconstruct all other components, the resultant encoding is biased towards information that is common across

all components. This bias towards commonality potentially undermines the model's ability to capture and represent the diversity inherent in multi-component datasets.

The mix of experts' products (MoPoE) framework [15] refines and generalizes the aggregation strategies of PoE and MoE, combining the precise joint posterior approximation of PoE with the improved learning of component-specific posteriors by MoE. The MoPoE model is designed to enhance multi-component learning by integrating these traits. Despite its conceptual advancements, the MoPoE model introduces a computational challenge due to its training strategy. It necessitates the evaluation of all conceivable component subsets, which equates to $2^M - 1$ training configurations for M components. This comprehensive strategy, while beneficial for robust learning across varied component combinations, leads to an exponential increase in computational requirements relative to the number of components. This aspect marks a significant limitation, especially for applications involving a large number of components.

To mitigate the averaging problem observed in mixture-based models, several studies [14], [16] have adopted component-specific latent spaces. Specifically, [14] identifies a 'shortcut' phenomenon, characterized by information predominantly circulating within component-specific subspaces. To address this, an enhancement of [8]'s model incorporates component-specific latent spaces designed exclusively for self-reconstruction. This strategy prevents the 'shortcut' by using a shared latent space to aggregate and a component-specific space to reconstruct unobserved components, ensuring that only joint information is retained in the shared space. Despite this advancement over prior approaches by resolving the shortcut dilemma, the outlined method introduces a training procedure that encompasses both reconstruction and cross-reconstruction tasks for each component pairing, leading to a computational requirement of M^2 forward passes for M components.

B. Markov Random Fields

Undirected Graphical Models, also called Markov Random Fields [9], [17], [18], were introduced to probability theory as a way to extend Markov processes from a temporal framework to a spatial one; they represent a stochastic process that has its origins in statistical physics [19]. Graphical models, including MRF, are notoriously hard to train due to the intractability of the partition function. This has led to numerous studies [20]–[24] aimed at developing more efficient methods for learning graphical models, including MRF.

C. MRF in Machine Learning

Markov Random Fields have predominantly been used in image processing tasks such as image deblurring [25], completion, texture synthesis, and image inpainting [26], as well as segmentation [27], [28]. However, recent advancements in more efficient methodologies have led to a decline in the use of MRF, due to the relative complexity involved in their learning processes.

To the best of our knowledge, there are limited instances where Markov Random Fields have been integrated within generative neural networks. Among these, [29] introduced the Structured Variational AutoEncoder (SVAE), which combines Conditional Random Fields with Variational AutoEncoders to address a variety of data modeling challenges. The SVAE has been applied to discrete mixture models, latent linear dynamical systems for video data, and latent switching linear dynamical systems for behavior analysis in video sequences. This approach employs mean field variational inference to approximate the Evidence Lower Bound, targeting specific data types without explicitly focusing on inter-component relationships.

Similarly, [30] integrates Boltzmann Machines as priors within VAEs, focusing on discrete variables to model complex and multi-component distributions. Their methodology suggests either factorial or hierarchical structures for the posterior distribution, aiming to effectively model complex and multi-component distributions.

Although significant advances have been made, the application of MRF within the domain of multi-component generative models, particularly in enhancing the integration and modeling of complex dependencies among multiple components remains largely unexplored. Our work seeks to bridge this gap by proposing a novel integration of MRF within a Multi-Component Variational AutoEncoder framework, aimed at capturing the intricate inter-component relationships more effectively. This approach not only leverages the strengths of MRF but also addresses the limitations observed in existing multi-component generative models.

III. METHODS

We define $\mathbf{X} = (\mathbf{x}_1, \dots, \mathbf{x}_M)$ as a collection of M random variables, each representing a distinct component. Our approach employs a Multi-Component Variational AutoEncoder with an integrated Markov Random Field in its latent space, specifically designed to effectively capture the complex inter-component relationships.

A. Variational AutoEncoders

Variational AutoEncoders (VAEs) [31], are generative models that use variational inference to handle an otherwise intractable posterior distribution $p(\mathbf{z}|\mathbf{X})$. Rather than directly optimizing the marginal log-likelihood, VAEs maximize an Evidence Lower Bound (ELBO), defined as:

$$\text{ELBO} = \mathbb{E}_{q_\phi(\mathbf{z}|\mathbf{X})} [\ln p_\theta(\mathbf{X} | \mathbf{z})] - \text{KL}(q_\phi(\mathbf{z} | \mathbf{X}) \parallel p(\mathbf{z})). \quad (1)$$

A VAE comprises two parts: an encoder, with parameters ϕ , that defines a variational distribution $q_\phi(\mathbf{z}|\mathbf{X})$ approximating the true posterior, and a decoder, with parameters θ , that specifies the likelihood $p_\theta(\mathbf{X} | \mathbf{z})$ mapping latent variables \mathbf{z} back to observed data \mathbf{X} .

B. Markov Random Fields

MRFs offer an intuitive framework to model inter-component dependencies, with nodes representing random variables and edges capturing their relationships.

Mathematically, an MRF is defined over an undirected graph $G = (V, E)$ where each node corresponds to a random variable in the set $(\mathbf{z}) = \{\mathbf{z}_i\}_{i=1}^n$. The joint distribution over these random variables is specified in terms of potential functions over cliques (fully connected subgraphs) of G . A general mathematical definition of an MRF is given by [18]:

$$p_{\text{MRF}} = \frac{1}{\mathcal{Z}} \exp \left[- \sum_{C \in \mathcal{C}} \psi_C(\mathbf{z}_C) \right] \quad (2)$$

where \mathcal{C} is the set of cliques in the graph, ψ_C are the potential functions that map configurations of the random variables within the clique to a real number, \mathbf{z}_C denotes the set of random variables in clique C , and \mathcal{Z} is the partition function that normalizes the distribution. In the context of our work, we model both the prior $p(\mathbf{z})$ and the posterior $q_\phi(\mathbf{z}|\mathbf{x}_1, \dots, \mathbf{x}_M)$ as fully connected MRF represented by unary $\psi_i(\mathbf{z}_i)$ and pairwise $\psi_{i,j}(\mathbf{z}_i, \mathbf{z}_j)$ potentials. This leads to the specific form:

$$p_{\text{MRF}}(\mathbf{z}) = \frac{1}{\mathcal{Z}} \exp \left[- \left(\sum_{i < j}^M \psi_{i,j}(\mathbf{z}_i, \mathbf{z}_j) + \sum_i^M \psi_i(\mathbf{z}_i) \right) \right] \quad (3)$$

with $\mathbf{z} = (\mathbf{z}_1, \dots, \mathbf{z}_M)$. This formulation enables the modeling of dependencies between components in our multi-component VAE framework by leveraging the structure of MRFs to capture both local and global interactions within the latent space.

C. General MRF MCVAE Architecture and the Gaussian Assumption

1) *General Framework*: In order to incorporate the MRF representation into a multi-component VAE framework, we employ the architecture illustrated in Figure 1. Each component \mathbf{x}_i is paired with an encoder-decoder structure: the component-specific encoder outputs the parameters of the unary potentials ψ_i , while a global encoder produces the pairwise potentials $\psi_{i,j}$. Together, these potentials define the joint posterior $q_\phi(\mathbf{z}|\mathbf{x}_1, \dots, \mathbf{x}_M)$, capturing both individual component details and their relationships. The latent variable $\mathbf{z} = (\mathbf{z}_1, \dots, \mathbf{z}_M)$ is sampled from this posterior and decomposed into sub-vectors \mathbf{z}_i , which are then reconstructed by their respective decoders.

However, the MRF framework introduces two significant challenges: First, computing the partition function \mathcal{Z} , which is necessary to normalize the joint distribution, is computationally expensive in fully connected MRFs; and second, sampling from generalized MRFs is inherently complex, making it difficult to integrate into gradient-based optimization.

To address these challenges, one could use sampling methods such as Hamiltonian Monte Carlo to estimate the ELBO without directly computing \mathcal{Z} , although this sacrifices end-to-end differentiability. Alternatively, the gradient of the ELBO can be approximated by explicitly estimating $\log \mathcal{Z}$ [30], albeit at a significant computational cost. These limitations restrict the scalability of fully unconstrained MRFs in large-scale applications.

2) *GMRF MCVAE*: These challenges lead us to adopt a simpler Gaussian assumption, achieving a balance between expressivity and tractability. In particular, we approximate both the prior and posterior using a Gaussian Markov Random Field, which avoids costly partition function calculations and enables a straightforward, differentiable sampling mechanism via the reparameterization trick.

Adopting the standard GMRF notation [18], the unary and pairwise potentials become:

$$\psi_i(\mathbf{z}_i) = \exp \left(-\frac{1}{2} \mathbf{z}_i^\top \Lambda_{i,i} \mathbf{z}_i + \eta_i^\top \mathbf{z}_i \right) \quad (4)$$

$$\psi_{i,j}(\mathbf{z}_i, \mathbf{z}_j) = \exp \left(-\frac{1}{2} \mathbf{z}_i^\top \Lambda_{i,j} \mathbf{z}_j \right) \quad (5)$$

and the joint distribution in natural form is

$$p_{\text{GMRF}}(\mathbf{z}) \propto \exp \left(\eta^\top \mathbf{z} - \frac{1}{2} \mathbf{z}^\top \Lambda \mathbf{z} \right) \quad (6)$$

Here, Λ is the precision matrix, partitioned into blocks $\Lambda_{i,j} \in \mathbb{R}^{d \times d}$, and $\eta = (\eta_1, \dots, \eta_M)$, with each $\eta_i \in \mathbb{R}^d$. Together, Λ and η define the natural parameters of the Gaussian distribution $p(\mathbf{z})$, where $\mathbf{z} = (\mathbf{z}_1, \dots, \mathbf{z}_M)$.

Rather than working directly with Λ , we find it more convenient to use its inverse. Defining $\mu = \Lambda^{-1}\eta$ and $\Sigma = \Lambda^{-1}$, we obtain the standard multivariate Gaussian:

$$p_{\text{GMRF}}(\mathbf{z}) = \frac{1}{(2\pi)^{\frac{Md}{2}} |\Sigma|^{\frac{1}{2}}} \exp \left(-\frac{1}{2} (\mathbf{z} - \mu)^\top \Sigma^{-1} (\mathbf{z} - \mu) \right) \quad (7)$$

which simplifies both conceptual understanding and computational tasks such as sampling. This parameterization thus provides a practical way to embed GMRF within our multi-component VAE framework.

3) *Differentiable Sampling*: A key advantage of the GMRF formulation is its compatibility with efficient gradient-based optimization, thanks to the reparameterization trick. By applying the Cholesky factorization $\Sigma = L L^\top$ [32], we rewrite a sample \mathbf{z} as:

$$\mathbf{z} = \mu + L \mathbf{u}, \quad \mathbf{u} \sim \mathcal{N}(\mathbf{0}, \mathbf{I}) \quad (8)$$

thus guaranteeing $\mathbf{z} \sim \mathcal{N}(\mu, \Sigma)$. Since both μ and L are learnable functions of the network parameters, this \mathbf{z} -sampling process is fully differentiable, enabling efficient backpropagation through the latent space.

4) *Conditional Generation*: The GMRF assumption also simplifies conditional sampling. In a multivariate Gaussian distribution, conditioning on any subset of variables yields another Gaussian in closed form. Specifically, let $\mathbf{z} = (z_1, \dots, z_n) \sim \mathcal{N}(\mu, \Sigma)$, where $\mu = (\mu_1, \dots, \mu_n)$ and Σ is partitioned into blocks $\Sigma_{i,j}$. Then, for indices $i \neq j$,

$$p(\mathbf{z}_i | \mathbf{z}_j = z_j) = \mathcal{N}(\hat{\mu}_i, \hat{\Sigma}_{i,i}) \quad (9)$$

with

$$\hat{\mu}_i = \mu_i + \Sigma_{i,j} \Sigma_{j,j}^{-1} (z_j - \mu_j), \quad \hat{\Sigma}_{i,i} = \Sigma_{i,i} - \Sigma_{i,j} \Sigma_{j,j}^{-1} \Sigma_{i,j}^\top$$

A full proof is provided in Appendix A. In practice, this closed-form property lets us generate specific components \mathbf{z}_i conditioned on partial observations \mathbf{z}_j without further training or approximation.

5) *Covariance Matrix Construction in the GMRF MCVAE:* To incorporate Gaussian Markov Random Fields (GMRFs) into the multi-component VAE (MCVAE) posterior, we parameterize the latent covariance matrix Σ as a block matrix:

$$\Sigma = \begin{bmatrix} \Sigma_{1,1} & \cdots & \Sigma_{1,M} \\ \vdots & \ddots & \vdots \\ \Sigma_{M,1} & \cdots & \Sigma_{M,M} \end{bmatrix}, \quad (10)$$

where $\Sigma_{i,i} \in \mathbb{R}^{d \times d}$ represents the component-specific variance matrices generated directly by the component-specific encoders. For $i \neq j$, the cross-component covariance matrices $\Sigma_{i,j} \in \mathbb{R}^{d \times d}$ are derived based on outputs from the global encoder, which are subsequently transformed to ensure symmetry and positive definiteness.

We propose a method to construct Σ as a symmetric positive definite (SPD) matrix, leveraging the following theorem, which generalizes the classical Hadamard corollary—linking strictly diagonally dominant matrices to positive definiteness—to the block matrix setting:

Theorem 1. Consider a block matrix Σ as defined in Equation 11. If for each $i \in \{1, \dots, M\}$ $\Sigma_{i,i}$ is SPD and satisfies:

$$\|\Sigma_{i,i}^{-1}\|^{-1} \geq \sum_{k \neq i} \|\Sigma_{i,k}\|$$

where $\|\cdot\|$ is the spectral norm, then Σ is also SPD.

The proof is detailed in Appendix B. This theorem forms the basis of the following SPD matrix construction:

- 1) **Diagonal Blocks:** Each component-specific encoder produces and SPD $\Sigma_{i,i}$.
- 2) **Off-Diagonal Blocks:** The global encoder outputs the off-diagonal blocks $\tilde{\Sigma}_{i,j} \in \mathbb{R}^{d \times d}$, capturing relationships between components. By symmetry, $\tilde{\Sigma}_{j,i} = \tilde{\Sigma}_{i,j}^\top$. Stacking these blocks yields:

$$\tilde{\Sigma} = \begin{bmatrix} 0 & \cdots & \tilde{\Sigma}_{1,M} \\ \vdots & \ddots & \vdots \\ \tilde{\Sigma}_{M,1} & \cdots & 0 \end{bmatrix} \quad (11)$$

- 3) **Scaling for Positive Definiteness:** To preserve diagonal dominance and ensure positive definiteness, each block row i is scaled using:

$$s_i = \sum_{\substack{j=1 \\ j \neq i}}^M \|\tilde{\Sigma}_{i,j}\| + \delta, \quad \alpha_i = \min\left(1, \epsilon \frac{\|\Sigma_{i,i}^{-1}\|^{-1}}{s_i}\right)$$

Here, $\delta > 0$ is a small constant to ensure numerical stability, and $\epsilon < 1$ is a hyperparameter. We then compute the scaled off-diagonal blocks as:

$$\Sigma_{i,j} = \tilde{\Sigma}_{i,j} \cdot \sqrt{\alpha_i \alpha_j}$$

- 4) **Matrix Assembly:** The final covariance matrix Σ is assembled as:

$$\Sigma = (\Sigma_{i,j})_{i,j}$$

This construction ensures that Σ remains symmetric and positive definite while effectively modeling components interactions. However, the block-wise method incurs a computational overhead of $\mathcal{O}(M^2 d^3)$. By applying the construction element-wise, the complexity is reduced to $\mathcal{O}(M^2 d^2)$ ¹. Nevertheless, conditional generation using Equation 9 requires each component-specific covariance $\Sigma_{j,j}$ to be self-contained, i.e., independently derivable using only encoder j . The variance construction method disrupts this independence. To address this limitation, we adopt the simplifying assumption that $\Sigma_{j,j}$ are diagonal matrices.

IV. EXPERIMENTS

We benchmark the proposed GMRF MCVAE against four leading multi-component Variational AutoEncoders: MVAE [7], MMVAE [8], MoPoE-VAE [15], and MMVAE+ [14]. The core objective is to evaluate the models' ability to learn and preserve complex inter-component structure.

a) *Copula Dataset.*: To emphasize dependency modeling rather than component complexity, we design a synthetic dataset based on Gaussian Copulas. Each sample consists of multiple components that are individually drawn from uniform distributions $\mathcal{U}([0, 1])$, but exhibit intricate interactions via a Gaussian Copula. This setup emulates real-world dependencies observed in domains like finance [33] or weather events [34], ensuring that capturing cross-component relationships is the primary challenge.

b) *PolyMNIST Benchmark.*: We further evaluate all models on PolyMNIST, a widely used benchmark in multimodal generative modeling [15]. PolyMNIST introduces more complex individual components—digit images but maintains relatively simple inter-component dependencies, as all five modalities correspond to the same digit.

c) *BIKED Dataset.*: Traditional multimodal benchmarks enforce simplified coherence constraints, such as digit consistency in PolyMNIST. However, real-world applications require generative models that capture complex structural dependencies. In structured systems like industrial design, coherence extends beyond semantic alignment to include spatial and functional constraints that ensure plausibility within a given domain. For example, in a fabrication pipeline, a designer must generate components that seamlessly integrate into an assembly while maintaining geometric and functional integrity. Unlike standard multimodal benchmarks that focus on feature consistency, industrial datasets exhibit strong interdependencies between components, requiring models to generate structurally valid outputs rather than just visually plausible ones. To evaluate generative models in this setting, we use BIKED [35], an open-source dataset of bicycle designs particularly well-suited for partial-to-full generation in a multi-component environment.

¹A detailed comparison (App. D) shows that, even with this extra $\mathcal{O}(M^2 d^2)$ term, the overall training cost remains lower than that of other baselines.

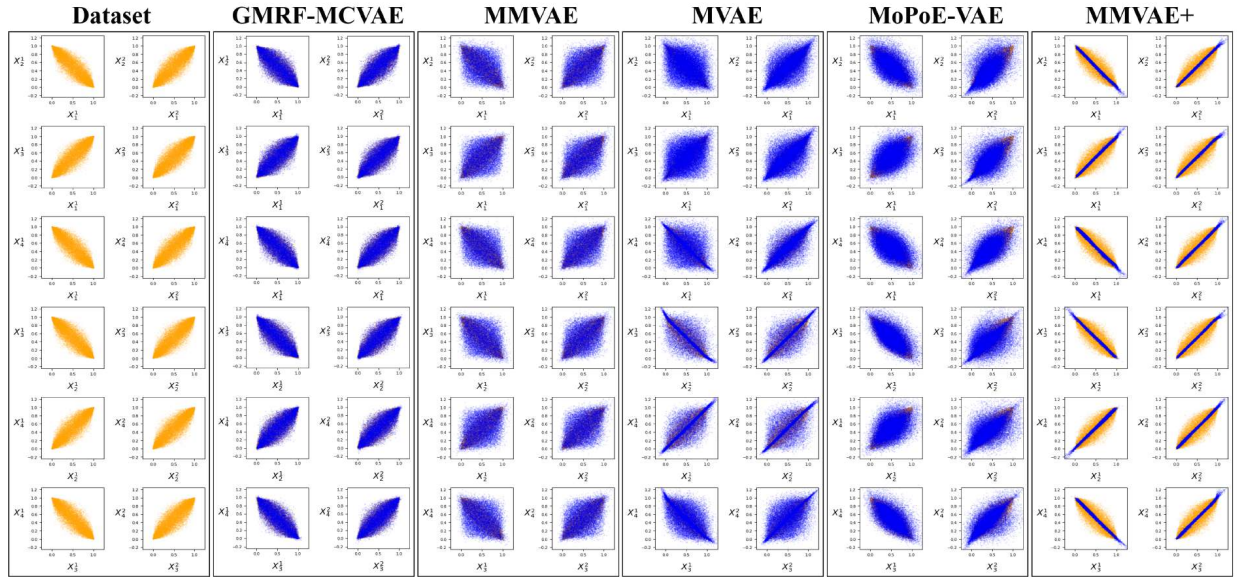


Fig. 2. Qualitative results for the unconditional generations on the Copula dataset. Each subplot visualizes joint distributions for each pair of coordinates (x_i^1, x_j^1) and (x_i^2, x_j^2) across the four two-dimensional components (x_1, x_2, x_3, x_4) . The true distributions are depicted in orange and the generated ones in blue.

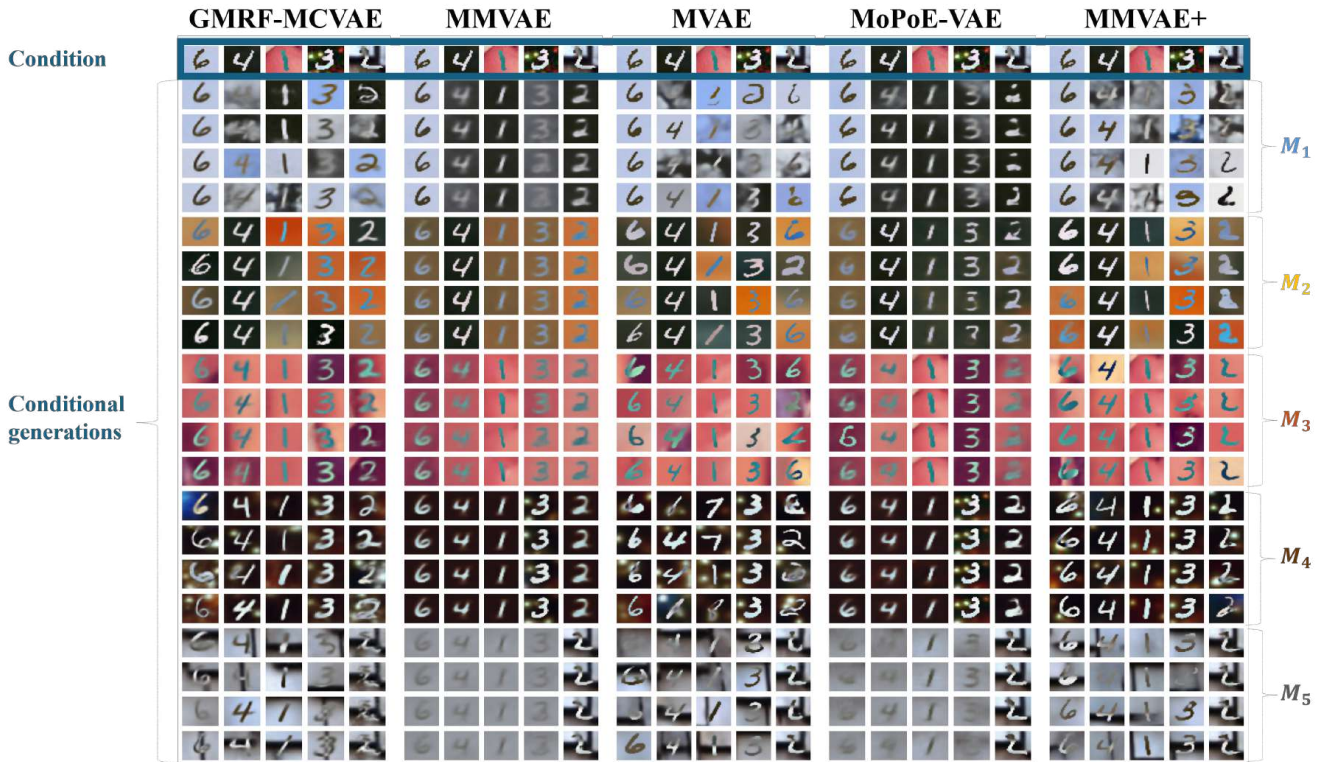


Fig. 3. PolyMNIST conditional generations. Each block corresponds to a model. In each column, the first image corresponds to the condition, followed by the conditionally generated components M_i .

We average all numerical results over three independently trained models. Training details, including architectures and hyperparameters, are provided in the Appendix C.

A. Copula Dataset Evaluation

This subsection evaluates the capability of each model to handle and represent complex inter-component interactions. The synthetic dataset consists of four two-dimensional com-

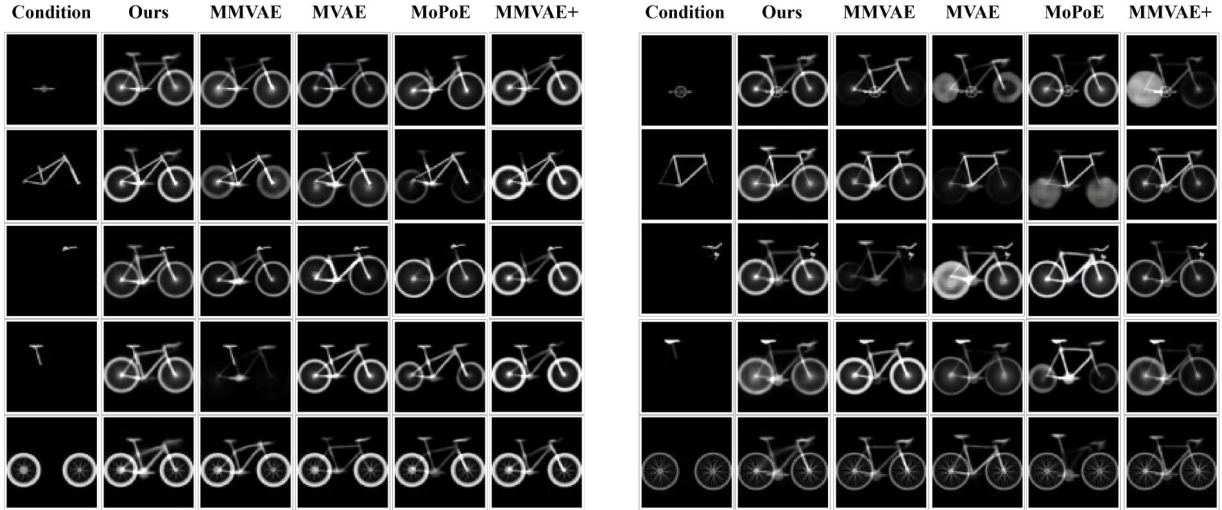


Fig. 4. Conditional generation on BIKED. The first column shows the conditioning components, while each subsequent column presents the remaining generated components for each model, overlaid to form the complete bike.

Model	Uncond. Gen.			Cond. Gen.		
	Dim 1	Dim 2	Mean	Dim 1	Dim 2	Mean
MVAE	2.7	3.2	2.9	3.0	3.1	3.1
MMVAE	5.2	4.5	4.8	5.4	4.7	5.0
MoPoE-VAE	1.9	2.6	2.2	6.0	5.6	5.9
MMVAE+	8.1	4.9	6.5	5.2	4.9	5.1
GMRF MCVAE	0.7	0.95	0.86	2.6	2.7	2.6

TABLE I

COMPARATIVE RESULTS ON THE SYNTHETIC COPULA DATASET FOR UNCONDITIONAL (UNCOND.) AND CONDITIONAL (COND.) GENERATION USING SCALED WASSERSTEIN DISTANCES (MULTIPLIED BY 1000).

ponents, $\mathbf{x}_1, \mathbf{x}_2, \mathbf{x}_3, \mathbf{x}_4$, each defined as $\mathbf{x}_i = (\mathbf{x}_i^1, \mathbf{x}_i^2)$ where each component \mathbf{x}_i^j is uniformly distributed, $\mathbf{x}_i^j \sim \mathcal{U}([0, 1])$, for $i \in \{1, 2, 3, 4\}$ and $j \in \{1, 2\}$. The coordinates of each component are generated using two Gaussian Copulas, $C_j(\mathbf{x}_1^j, \dots, \mathbf{x}_4^j)$, with uniform means $\mu_j = [3, \dots, 3]$ and standard deviations $\sigma_j = [1, \dots, 1]$. The correlation matrices R^j have off-diagonal elements set as $R_{k,l}^j = ((-1)^j)^{k+l} \cdot 0.9$ (cf. Figure 2).

a) *Metric*: We assess model performance using the Wasserstein distance [36], which measures the optimal transport cost between the empirical probability density functions (PDFs) of the generated and true samples for each component’s coordinates. This metric captures differences in both the supports and shapes of distributions. The average of these distances across all comparisons serves as an aggregate performance measure.

1) *Qualitative Comparison*: In the analysis of joint distributions (Figure 2), the GMRF MCVAE demonstrates superior alignment with the true distribution, indicating high-quality generations. The MVAE captures certain inter-component relationships more effectively, although this varies across components. Notably, the third component appears less accurate. This variability is explored in further detail in appendix E. As noted by [8], this may stem from the “veto” effect, where experts with higher precision dominate the joint posterior, leading

to biased predictions. The MoPoE-VAE combines features of both the MVAE and MMVAE, producing less noisy images but failing to consistently enforce cross-component relationships. Notably, MMVAE+ underperforms compared to other models. While it captures the general correlation between components, it struggles to model the complete dependency structure of the true distribution. This may be due to the increased complexity introduced by component-specific sampling, which complicates the representation of intricate inter-component dependencies.

2) *Quantitative Comparison*: Table I confirms the observations from the previous section. The Wasserstein distances between the true and generated distribution PDFs indicate that the GMRF MCVAE generates distributions closer to the true distributions.

B. PolyMNIST Dataset Evaluation

Model	Unconditional		Conditional		
	FID	Coherence	FID	Coherence	SSIM
MVAE	95.14	0.139	94.71	0.448	0.993
MMVAE	170.87	0.175	198.80	0.517	0.995
MoPoE-VAE	106.12	0.018	162.74	0.475	0.995
MMVAE+	87.23	0.210	82.05	0.856	0.994
GMRF MCVAE	118.21	0.321	180.76	0.869	0.995

TABLE II

RESULTS ON POLYMNIST SHOWING FID, COHERENCE, AND SSIM FOR VARIOUS MODELS.

In this section, we present the results of our evaluation on the PolyMNIST dataset, assessing the models’ ability to handle component complexity and ensure consistency across components. PolyMNIST [15] extends MNIST into a five-component dataset, where each data point consists of five label-consistent images of the same digit, rendered in distinct handwriting styles and paired with unique background types. This setup challenges models to capture the shared digit iden-

tity while managing the complexity introduced by handwriting and background variations.

a) Metrics: We evaluate model performance using the Fréchet Inception Distance (FID) [37], which measures generative quality and diversity [38], and the Structural Similarity Index (SSIM) [39], which assesses perceptual similarity between generated and real images. Additionally, we evaluate global coherence using the methodology proposed by Palumbo et al. [14], which measures whether all generated components share the same digit.

b) Qualitative Comparison: We observe that The GMRF MCVAE model produces consistently complete digits, though slightly blurrier than the MMVAE+ and MVAE (cf Figure 3). The MVAE generates sharp images but struggles to align digit identities across components, likely due to the conditional independence assumption induced by the PoE aggregation. MMVAE however suffers from an averaging effect, which dilutes component-specific details and leads to blend backgrounds and a lack of digit variability. MoPoE-VAE by construction attempts to balance PoE and MoE, but visually exhibits their combined drawbacks: oversmoothing and incomplete digits. Despite some trade-offs in sharpness, our GMRF MCVAE consistently preserves the coherence and diversity of the digits, ensuring high generative quality and semantic coherence.

c) Quantitative Comparison: The quantitative evaluation, as presented in Table II, reveals that the GMRF MCVAE model performs competitively across all considered metrics on the PolyMNIST dataset. Although the MVAE model achieves the lowest FID scores, the GMRF MCVAE exhibits higher values of cross-coherence and SSIM, suggesting enhanced preservation of structural integrity and global coherence in the generated samples. These results underscore the GMRF MCVAE’s ability to produce high-quality, structurally coherent outputs, indicating its robustness in multi-component generative modeling.

C. BIKED Evaluation

BIKED [35] dataset is a collection of 4,500 bicycle models designed by hundreds of designers, originally introduced for data-driven bicycle design applications. The dataset includes various types of design information, such as parametric data, class labels, and images of full bike assemblies and individual components. In this work, we focus on the segmented component images, where each image corresponds to a different part of a bicycle. Specifically, we retain only the five essential components—saddle, frame, crank, wheels, and handlebars, while discarding components that do not consistently appear across all images, such as water bottles and cargo racks. To reduce GPU load and accelerate training, we convert all images to grayscale and downsample them to 64×64 resolution.

a) Metrics: We evaluated generation quality and diversity using FID and structural coherence with SSIM, which measures how well the overall structure of conditionally generated bikes aligns with real ones. While SSIM provides a perceptual evaluation of global shape consistency, industrial design often requires more domain-specific geometric

constraints to ensure practical feasibility, e.g., maintaining an appropriate crank-to-wheel distance for maneuverability. To capture such structural dependencies in a scalable and generalizable manner, we propose the Wasserstein distance between component centers of mass, which quantifies the global spatial distribution of parts. This approach enables us to assess whether the generated components form structurally plausible assemblies, independent of predefined expert rules, making it applicable to other industrial multi-component datasets.

1) Qualitative comparison: Qualitative results of conditional generation (Figure 4) highlight the limitations of the baseline models. Although MVAE, MMVAE, and MoPoE-VAE exhibit high variability by mixing components from different types of bikes, their generated outputs often lack structural integrity. Specifically, the outputs frequently contain missing or incomplete components, and MVAE, in particular, produces structurally infeasible designs, such as misaligned rear frame sections, causing the rear wheel to be improperly positioned, making the generated bikes impractical for real-world assembly. MMVAE+ demonstrates better structural consistency, as its generations more closely resemble complete and coherent bicycles when conditioned on specific components. However, this comes at the cost of reduced variability, and we observe frequent missing components, such as absent saddles. Our model, by contrast, achieves a balance between variability and structural integrity. While its generations may not be as diverse as those of MVAE, they remain structurally coherent and plausible as functional bicycle designs, aligning with expected industrial feasibility.

2) Quantitative comparison: The results in Table III align with our qualitative observations. MVAE, MMVAE, and MoPoE-VAE achieve the lowest FID scores, indicating higher diversity in their generations. However, our model maintains competitive FID performance while achieving the best SSIM and Wasserstein distance scores, confirming its ability to generate structurally coherent designs. Higher SSIM values indicate that our model better preserves local structural consistency in conditional generations, ensuring that the generated components align more closely with real designs. Additionally, the significantly lower Wasserstein distance between the center of mass of the components suggests superior spatial integrity, meaning that the generated parts are correctly positioned relative to each other. This supports our model’s ability to balance diversity with structural plausibility, producing generations that are not only varied but also geometrically coherent and physically plausible.

V. CONCLUSION

This work addressed a core limitation of current multi-component generative models: their inability to explicitly capture dependencies between components. We introduced GMRF MCVAE, a Variational AutoEncoder architecture that integrates Gaussian Markov Random Fields within both prior and posterior distributions, enabling structured latent spaces that model cross-component relationships directly.

Model	Unconditional		Conditional				
	Comp. FID	Full. FID	Comp. FID	Full. FID	Comp. SSIM	Full. SSIM	WS
MVAE	136.60	155.06	134.78	151.77	0.85	0.53	0.46
MMVAE	133.59	148.34	132.45	146.92	0.84	0.50	0.47
MoPoE-VAE	136.29	158.25	131.94	150.44	0.85	0.53	0.49
MMVAE+	137.17	176.12	131.78	171.48	0.84	0.54	0.51
GMRF MCVAE (ours)	136.83	186.88	131.52	173.70	0.88	0.64	0.31

TABLE III

COMPARISON OF FID, SSIM AND WASSERSTEIN DISTANCE (WS) METRICS FOR COMPONENT-WISE (COMP.) AND FULL-BIKE (FULL.) GENERATIONS ACROSS MODELS. LOWER FID AND WS VALUES INDICATE BETTER PERFORMANCE, WHILE HIGHER SSIM VALUES REFLECT GREATER STRUCTURAL SIMILARITY.

Our model achieved competitive results on PolyMNIST and outperformed state-of-the-art baselines on both the synthetic Copula dataset and the BIKED dataset, demonstrating its strength in tasks where structural coherence is essential. Notably, GMRF MCVAE generates assemblies that preserve both diversity and spatial integrity, a key requirement for real-world industrial design and multi-component generation tasks.

Looking forward, we aim to generalize this approach using sparse MRF structures to improve scalability, and to explore interpretability via the graphical representation of dependencies. Finally, incorporating domain-specific constraints into evaluation protocols will help bring this method closer to practical deployment in engineering and design workflows.

REFERENCES

- [1] D. Puhr-Westerheide, C. C. Cyran, J. Sargsyan-Bergmann, A. Tódica, F.-J. Gildehaus, W. G. Kunz, R. Stahl, C. Spitzweg, J. Ricke, and P. M. Kazmierczak, "The added diagnostic value of complementary gadoteric acid-enhanced mri to 18 f-dopa-pet/ct for liver staging in medullary thyroid carcinoma," *Cancer Imaging*, vol. 19, pp. 1–10, 2019.
- [2] A. Rahimi, A. Khalil, A. Faisal, and K. W. Lai, "Ct-mri dual information registration for the diagnosis of liver cancer: A pilot study using point-based registration," *Current medical imaging*, vol. 18, no. 1, pp. 61–66, 2022.
- [3] Q. Xie, W. Han, X. Zhang, Y. Lai, M. Peng, A. Lopez-Lira, and J. Huang, "Pixiu: A comprehensive benchmark, instruction dataset and large language model for finance," *Advances in Neural Information Processing Systems*, vol. 36, 2024.
- [4] S. I. Lee and S. J. Yoo, "Multimodal deep learning for finance: integrating and forecasting international stock markets," *The Journal of Supercomputing*, vol. 76, pp. 8294–8312, 2020.
- [5] A. Cobb, A. Roy, D. Elenius, F. Heim, B. Swenson, S. Whittington, J. Walker, T. Bapty, J. Hite, K. Ramani *et al.*, "Aircraftverse: a large-scale multimodal dataset of aerial vehicle designs," *Advances in Neural Information Processing Systems*, vol. 36, pp. 44 524–44 543, 2023.
- [6] F. Oubari, R. Meunier, R. Décatoire, and M. Mougeot, "A meta-vaes for multi-component industrial systems generation," in *Intelligent Computing*, K. Arai, Ed. Cham: Springer Nature Switzerland, 2024, pp. 234–251.
- [7] M. Wu and N. Goodman, "Multimodal generative models for scalable weakly-supervised learning," *Advances in neural information processing systems*, vol. 31, 2018.
- [8] Y. Shi, B. Paige, P. Torr *et al.*, "Variational mixture-of-experts autoencoders for multi-modal deep generative models," *Advances in neural information processing systems*, vol. 32, 2019.
- [9] D. Koller and N. Friedman, *Probabilistic graphical models: principles and techniques*. MIT press, 2009.
- [10] A. Vahdat and J. Kautz, "Nvae: A deep hierarchical variational autoencoder," *Advances in neural information processing systems*, vol. 33, pp. 19 667–19 679, 2020.
- [11] S. D. Mbacke, F. Clerc, and P. Germain, "Statistical guarantees for variational autoencoders using pac-bayesian theory," *Advances in Neural Information Processing Systems*, vol. 36, 2024.
- [12] M. Suzuki, K. Nakayama, and Y. Matsuo, "Joint multimodal learning with deep generative models," *arXiv preprint arXiv:1611.01891*, 2016.
- [13] R. Vedantam, I. Fischer, J. Huang, and K. Murphy, "Generative models of visually grounded imagination," *arXiv preprint arXiv:1705.10762*, 2017.
- [14] E. Palumbo, I. Daunhawer, and J. E. Vogt, "Mmvae+: Enhancing the generative quality of multimodal vaes without compromises," in *The Eleventh International Conference on Learning Representations*. OpenReview, 2023.
- [15] T. M. Sutter, I. Daunhawer, and J. E. Vogt, "Generalized multimodal elbo," *arXiv preprint arXiv:2105.02470*, 2021.
- [16] T. Sutter, I. Daunhawer, and J. Vogt, "Multimodal generative learning utilizing jensen-shannon-divergence," *Advances in neural information processing systems*, vol. 33, pp. 6100–6110, 2020.
- [17] M. J. Wainwright, M. I. Jordan *et al.*, "Graphical models, exponential families, and variational inference," *Foundations and Trends® in Machine Learning*, vol. 1, no. 1–2, pp. 1–305, 2008.
- [18] K. P. Murphy, *Machine learning: a probabilistic perspective*. MIT press, 2012.

- [19] R. Kindermann and J. L. Snell, *Markov random fields and their applications*. American Mathematical Society, 1980, vol. 1.
- [20] M. A. Carreira-Perpinan and G. Hinton, "On contrastive divergence learning," in *International workshop on artificial intelligence and statistics*. PMLR, 2005, pp. 33–40.
- [21] M. Vuffray, S. Misra, and A. Lokhov, "Efficient learning of discrete graphical models," *Advances in Neural Information Processing Systems*, vol. 33, pp. 13 575–13 585, 2020.
- [22] F. Bach and M. Jordan, "Learning graphical models with mercer kernels," *Advances in Neural Information Processing Systems*, vol. 15, 2002.
- [23] K. M. Tan, P. London, K. Mohan, S.-I. Lee, M. Fazel, and D. Witten, "Learning graphical models with hubs," *arXiv preprint arXiv:1402.7349*, 2014.
- [24] M. Welling and C. Sutton, "Learning in markov random fields with contrastive free energies," in *International Workshop on Artificial Intelligence and Statistics*. PMLR, 2005, pp. 397–404.
- [25] P. Perez *et al.*, *Markov random fields and images*. IRISA, 1998, vol. 469.
- [26] N. Komodakis and G. Tziritas, "Image completion using efficient belief propagation via priority scheduling and dynamic pruning," *IEEE Transactions on Image Processing*, vol. 16, no. 11, pp. 2649–2661, 2007.
- [27] P. Krähenbühl and V. Koltun, "Efficient inference in fully connected crfs with gaussian edge potentials," *Advances in neural information processing systems*, vol. 24, 2011.
- [28] M. G. Bello, "A combined markov random field and wave-packet transform-based approach for image segmentation," *IEEE transactions on image processing*, vol. 3, no. 6, pp. 834–846, 1994.
- [29] M. J. Johnson, D. K. Duvenaud, A. Wiltchko, R. P. Adams, and S. R. Datta, "Composing graphical models with neural networks for structured representations and fast inference," *Advances in neural information processing systems*, vol. 29, 2016.
- [30] A. H. Khoshman and M. Amin, "Gumbolt: Extending gumbel trick to boltzmann priors," *Advances in Neural Information Processing Systems*, vol. 31, 2018.
- [31] D. P. Kingma and M. Welling, "Auto-encoding variational bayes," *arXiv preprint arXiv:1312.6114*, 2013.
- [32] D. P. Kingma, M. Welling *et al.*, "An introduction to variational autoencoders," *Foundations and Trends® in Machine Learning*, vol. 12, no. 4, pp. 307–392, 2019.
- [33] D. MacKenzie and T. Spears, "'the formula that killed wall street': The gaussian copula and modelling practices in investment banking," *Social Studies of Science*, vol. 44, no. 3, pp. 393–417, 2014.
- [34] P. Tedesco, A. Lenkoski, H. C. Bloomfield, and J. Sillmann, "Gaussian copula modeling of extreme cold and weak-wind events over europe conditioned on winter weather regimes," *Environmental Research Letters*, vol. 18, no. 3, p. 034008, 2023.
- [35] L. Regenwetter, B. Curry, and F. Ahmed, "Biked: A dataset for computational bicycle design with machine learning benchmarks," *Journal of Mechanical Design*, vol. 144, no. 3, p. 031706, 2022.
- [36] C. Villani, "The wasserstein distances," *Optimal Transport: Old and New*, pp. 93–111, 2009.
- [37] M. Heusel, H. Ramsauer, T. Unterthiner, B. Nessler, and S. Hochreiter, "Gans trained by a two time-scale update rule converge to a local nash equilibrium," *Advances in neural information processing systems*, vol. 30, 2017.
- [38] J. Ho and T. Salimans, "Classifier-free diffusion guidance," *arXiv preprint arXiv:2207.12598*, 2022.
- [39] Z. Wang, A. C. Bovik, H. R. Sheikh, and E. P. Simoncelli, "Image quality assessment: from error visibility to structural similarity," *IEEE transactions on image processing*, vol. 13, no. 4, pp. 600–612, 2004.
- [40] K. B. Petersen, M. S. Pedersen *et al.*, "The matrix cookbook," *Technical University of Denmark*, vol. 7, no. 15, p. 510, 2008.
- [41] D. G. Feingold and R. S. Varga, "Block diagonally dominant matrices and generalizations of the gerschgorin circle theorem." 1962.
- [42] I. Higgins, L. Matthey, A. Pal, C. P. Burgess, X. Glorot, M. M. Botvinick, S. Mohamed, and A. Lerchner, "beta-vae: Learning basic visual concepts with a constrained variational framework," *ICLR (Poster)*, vol. 3, 2017.

APPENDIX

A. Conditional Sampling

The conditional distribution of a normally distributed random variable given another is also normally distributed. This is known for the bivariate case in the Matrix Cookbook [40]. We extend this result for $n \geq 2$, considering a random vector $\mathbf{z} \sim \mathcal{N}(\boldsymbol{\mu}, \boldsymbol{\Sigma})$ with the following probability density function:

$$\mathbf{z} = \begin{pmatrix} \mathbf{z}_1 \\ \vdots \\ \mathbf{z}_n \end{pmatrix} \sim \mathcal{N} \left(\begin{pmatrix} \mu_1 \\ \vdots \\ \mu_n \end{pmatrix}, \begin{bmatrix} \Sigma_{11} & \cdots & \Sigma_{1n} \\ \vdots & \ddots & \vdots \\ \Sigma_{n1} & \cdots & \Sigma_{nn} \end{bmatrix} \right). \quad (12)$$

For any pair of indices $i \neq j$ from the set $\{1, \dots, n\}$, the conditional distribution of \mathbf{z}_i given \mathbf{z}_j is

$$p(\mathbf{z}_i | \mathbf{z}_j = \mathbf{z}_j) = \mathcal{N}(\hat{\mu}_i, \hat{\Sigma}_{i,i}), \quad (13)$$

where

$$\begin{cases} \hat{\mu}_i = \mu_i + \Sigma_{i,j} \Sigma_{j,j}^{-1} (\mathbf{z}_j - \mu_j), \\ \hat{\Sigma}_{i,i} = \Sigma_{i,i} - \Sigma_{i,j} \Sigma_{j,j}^{-1} \Sigma_{j,i}. \end{cases} \quad (14)$$

Proof. Consider a random vector \mathbf{z} and distinct indices i and j . Define the transformation $\mathbf{y} = A\mathbf{z}_i + B\mathbf{z}_j$ such that \mathbf{y} and \mathbf{z}_j are independent. To achieve $\text{cov}(\mathbf{y}, \mathbf{z}_j) = 0$, it follows that

$$A\Sigma_{i,j} + B\Sigma_{j,j} = 0.$$

Selecting $A = I$, leads to

$$B = -\Sigma_{i,j} \Sigma_{j,j}^{-1}.$$

Substituting back, we obtain

$$\mathbf{y} = \mathbf{z}_i - \Sigma_{i,j} \Sigma_{j,j}^{-1} \mathbf{z}_j.$$

The independence implies $\mathbf{E}[\mathbf{y} | \mathbf{z}_j] = \mathbf{E}[\mathbf{y}] = \mu_i$. Consequently, the conditional expectation of \mathbf{z}_i given \mathbf{z}_j is

$$\begin{aligned} \mathbf{E}[\mathbf{z}_i | \mathbf{z}_j] &= \mathbf{E}[\mathbf{y} + \Sigma_{i,j} \Sigma_{j,j}^{-1} \mathbf{z}_j | \mathbf{z}_j] \\ &= \mathbf{E}[\mathbf{y} | \mathbf{z}_j] + \Sigma_{i,j} \Sigma_{j,j}^{-1} \mathbf{z}_j \\ &= \mu_i + A(\mu_j - \mathbf{z}_j). \end{aligned}$$

For the variance, we derive:

$$\begin{aligned} \text{var}(\mathbf{z}_i | \mathbf{z}_j) &= \text{var}(\mathbf{y} - B\mathbf{z}_j | \mathbf{z}_j) \\ &= \text{var}(\mathbf{y} | \mathbf{z}_j) + \text{var}(B\mathbf{z}_j | \mathbf{z}_j) \\ &\quad - B\text{cov}(\mathbf{y}, -\mathbf{z}_j) - \text{cov}(\mathbf{y}, -\mathbf{z}_j) B' \\ &= \text{var}(\mathbf{y} | \mathbf{z}_j) \\ &= \text{var}(\mathbf{y}). \end{aligned}$$

Thus:

$$\begin{aligned} \text{var}(\mathbf{z}_i | \mathbf{z}_j) &= \text{var}(\mathbf{z}_i + B\mathbf{z}_j) \\ &= \text{var}(\mathbf{z}_i) + B\text{var}(\mathbf{z}_j) B' + B\text{cov}(\mathbf{z}_j, \mathbf{z}_i) \\ &\quad - \text{cov}(\mathbf{z}_i, \mathbf{z}_j) B' \\ &= \Sigma_{i,i} + B\Sigma_{j,j} B' - B\Sigma_{j,i} - \Sigma_{i,j} B' \\ &= \Sigma_{i,i} - \Sigma_{i,j} \Sigma_{j,j}^{-1} \Sigma_{j,i} \end{aligned}$$

This final expression for $\text{var}(\mathbf{z}_i | \mathbf{z}_j = \mathbf{z}_j)$ is the variance of the conditional distribution $p(\mathbf{z}_i | \mathbf{z}_j = \mathbf{z}_j) = \mathcal{N}(\hat{\mu}_i, \hat{\Sigma}_{i,i})$, where $\hat{\Sigma}_{i,i} = \Sigma_{i,i} - \Sigma_{i,j} \Sigma_{j,j}^{-1} \Sigma_{j,i}$. \square

B. Demonstration of Theorem 1

1) *Preliminaries*: This section demonstrates how our architecture can generate full diagonal block covariance matrices while ensuring symmetric positive definiteness.

Let M be a complex matrix, and let E and F be two vector spaces equipped with norms $\|\cdot\|_E$ and $\|\cdot\|_F$, respectively, such that for all $\mathbf{x} \in E$, $M\mathbf{x} \in F$.

The standard operator norm of M is defined as:

$$\|M\| = \sup_{\mathbf{x} \neq 0} \frac{\|M\mathbf{x}\|_F}{\|\mathbf{x}\|_E}.$$

Consider a block matrix Σ defined as:

$$\Sigma = \begin{bmatrix} \Sigma_{1,1} & \cdots & \Sigma_{1,n} \\ \vdots & \ddots & \vdots \\ \Sigma_{n,1} & \cdots & \Sigma_{n,n} \end{bmatrix}, \quad (15)$$

where $\Sigma_{i,i}$ are square matrices and $\Sigma_{i,j}$ for $i \neq j$ are rectangular matrices, all with complex entries. In the remainder of this section, we will refer to Σ as defined in Equation 15.

Following [41], we say that Σ is block diagonally dominant with respect to the norm $\|\cdot\|$ if:

$$\|\Sigma_{i,i}^{-1}\|^{-1} \geq \sum_{\substack{k=1 \\ k \neq i}}^n \|\Sigma_{i,k}\|, \quad \forall i \in \{1, \dots, n\}. \quad (16)$$

In order to prove Theorem 1, we need to present first the following two key theorems from [41]:

Theorem 2. A block matrix Σ is nonsingular if it is block strictly diagonally dominant (i.e., strict inequality holds in Equation 16).

Theorem 3. For a block matrix Σ , each eigenvalue λ satisfies:

$$(\|(\Sigma_{i,i} - \lambda \mathbf{I})^{-1}\|)^{-1} \leq \sum_{\substack{k=1 \\ k \neq i}}^n \|\Sigma_{i,k}\|,$$

for at least one $i \in \{1, \dots, n\}$.

2) Proof of Theorem 1:

Proof. To prove Theorem 1, we show that Σ is positive definite.

1. *Nonsingularity*: From Theorem 2, the block strictly diagonal dominance of Σ guarantees that it is nonsingular.

2. *Positivity*: Let λ be an eigenvalue of Σ . Theorem 3 ensures that there exists at least one $i \in \{1, \dots, n\}$ such that:

$$(\|(\Sigma_{i,i} - \lambda \mathbf{I})^{-1}\|)^{-1} \leq \sum_{\substack{k=1 \\ k \neq i}}^n \|\Sigma_{i,k}\|.$$

Since we consider in our theorem that $\|\cdot\|$ is the spectral norm, we have:

$$\|(\Sigma_{i,i} - \lambda \mathbf{I})^{-1}\| = \sup_{j \in \{1, \dots, d\}} \left| \frac{1}{\sigma_j^i - \lambda} \right|,$$

where $(\sigma_j^i)_j$ are the eigenvalues of $\Sigma_{i,i}$. Let $k \in \{1, \dots, d\}$ be the index where the supremum is achieved. Substituting this into the inequality gives:

$$(\|(\Sigma_{i,i} - \lambda \mathbf{I})^{-1}\|)^{-1} = |\sigma_k^i - \lambda|.$$

Using Theorem 2, we have:

$$|\sigma_k^i - \lambda| \leq \sum_{\substack{k=1 \\ k \neq i}}^n \|\Sigma_{i,k}\| < \|\Sigma_{i,i}^{-1}\|^{-1}.$$

For the spectral norm:

$$\|\Sigma_{i,i}^{-1}\| = \frac{1}{\sigma_{\min}^i},$$

where σ_{\min}^i is the smallest eigenvalue of $\Sigma_{i,i}$. Substituting into the inequality, we get:

$$|\sigma_k^i - \lambda| < \sigma_{\min}^i.$$

This implies:

$$-\sigma_{\min}^i + \sigma_k^i < \lambda < \sigma_{\min}^i + \sigma_k^i.$$

Since $-\sigma_{\min}^i + \sigma_k^i \geq 0$, it follows that $\lambda > 0$, proving that all eigenvalues of Σ are positive. And thus, Σ is SDP, completing the proof. \square

C. Technical details for the experiments

Throughout all the experiments, we train each model on 3 independent initializations. In this section we provide the experimental details for both PolyMNIST and the Copula experiments. The code and datasets used in our experiments will be made publicly available upon acceptance.

1) *PolyMNIST & BIKED Experiments*: We employ consistent encoder/decoder architectures across all baseline models, using publicly available implementations for MVAE, MMVAE, and MoPoE-VAE from [16], and for MMVAE+ from [14]. We use similar encoders/decoders architectures in both experiments with different parameters reported on table C2. Our GMRF MCVAE follows a similar ResNet-based design but differs in that we do not employ two separate latent spaces for joint and component specific encodings. Instead, we introduce an additional fully connected network (three layers of 128 ReLU units each, followed by a linear output) to generate the off-diagonal covariance blocks.

To ensure fair comparisons in both the PolyMNIST and BIKED tasks, we configure all factorized baseline models with a 32-dimensional latent space for PolyMNIST and an 8-dimensional latent space for BIKED (both split into shared and modality-specific subspaces). For unfactorized baselines, we use latent spaces of 512 dimensions for PolyMNIST and 16 dimensions for BIKED. In contrast, our GMRF MCVAE architecture employs a fixed latent space dimension of 16 for PolyMNIST and 4 for BIKED. Additionally, in the PolyMNIST experiment, we mask out 75% of the off-diagonal parameters in the covariance matrix of the GMRF MCVAE,

resulting in 660 parameters per distribution, to align with the effective latent capacity of the baselines.

All models are trained for 100 epochs and monitored using coherence and Fréchet Inception Distance (FID). For baseline models, we experiment with $\beta \in \{5, 2.5, 1\}$ (lower/higher beta values result in poorer performances). For the GMRF MCVAE in particular, we explore $\beta \in \{2.5 \times 10^{-3}, 1 \times 10^{-3}, 5 \times 10^{-4}, 1 \times 10^{-4}\}$, where β controls the KL term weight in the ELBO [42]. We find that $\beta = 1 \times 10^{-3}$ yields the best performance in both datasets.

2) *Copula Dataset Experiment*: Table IV presents the architecture details for both the encoders and decoders used in the Copula experiment. To maintain consistency in latent capacities across different models, the GMRF MCVAE was configured with a latent dimension of 2 (yielding a total capacity of 44), while all other models used a latent dimension of 3 (total capacity of 48). All models were trained for 200 epochs, exploring a range of β values: $\{2.5, 1, 0.1, 0.05, 0.001\}$. For baseline models, both Gaussian and Laplacian distributions were tested for the prior, posterior, and log-likelihood calculations. Factorized and unfactorized variants were evaluated for MVAE, MMVAE, and MoPoE-VAE.

D. Complexity comparison

Throughout this section we denote by

- M : the number of components (encoders/decoders);
- d : the dimensionality of each component-specific latent;
- C : the cost (forward and backward FLOPs) of a single decoder pass on one mini-batch.

a) *Per-step complexities*: Three baselines considered in our experiments have the following dominant costs:

- **MMVAE / MMVAE⁺**: M^2 cross-reconstructions $\implies \mathcal{O}(M^2 C)$.
- **MoPoE-VAE**: enumeration of 2^M modality subsets $\implies \mathcal{O}(2^M C)$.
- **GMRF MCVAE (ours)**: one $(Md)^2$ covariance build plus M self-decodes

$$\mathcal{O}(M^2 d^2 + M C).$$

After Σ is built, all cross-component generations are obtained by closed-form Gaussian conditioning; no extra decoder passes are required during training.

b) *When is our method competitive?*: Because MoPoE-VAE has an exponential cost $\mathcal{O}(2^M C)$, it is already asymptotically dominated by the polynomial budgets considered here. We equal the MMVAE/MMVAE⁺ budget when

$$M^2 d^2 + M C < M^2 C \implies C > \frac{M d^2}{M - 1}, \quad (17)$$

Dataset	M	d	Threshold on C
Copula	4	2	$C > 5.3$
PolyMNIST	5	16	$C > 320$
BIKED	5	4	$C > 20$

TABLE IX

NUMERICAL THRESHOLDS OBTAINED FROM (17) FOR THE THREE EXPERIMENTAL SETTINGS. FOR REFERENCE, TWO FULLY-CONNECTED LAYERS OF SIZE 256×256 ALREADY COST $\sim 2 \times 10^5$ FLOPS, FAR ABOVE ANY THRESHOLD LISTED.

Even though GMRF MCVAE incurs an $\mathcal{O}(M^2 d^2)$ covariance step, realistic decoders (convolutional or large FC) comfortably exceed the thresholds in Table IX, making our approach more efficient than the 3 baselines while still enabling closed-form partial-to-full generation.

E. Additional Results from the Copula Experiment

a) *Marginal Distributions*: As shown in Figure 5, the marginal generations from the various baseline models and the GMRF MCVAE, generally conform to the expected range. Notably, the GMRF MCVAE closely matches the empirical marginal distributions of the dataset, consistently producing outputs within the defined range of $[0, 1]$.

b) *Unconditional MVAE Generations*: Figure 6 displays the MVAE results after three independent training iterations, revealing inconsistent alignment with the actual joint distributions between components. The MVAE tends to focus selectively on certain components, often overlooking others. This behavior reflects the "veto" effect described in [8], where overconfident experts disproportionately influence the model's output. Such biases negatively impact the global coherence, compromising the accurate representation of inter-component relationships.

F. Exploring a Generalized Variant of GMRF MCVAE Models

In this section, we discuss a more comprehensive configuration in which both the prior $p(\mathbf{z})$ and posterior $p(\mathbf{z}|\mathbf{X})$ are characterized by general Markov Random Fields. This approach opens up possibilities for robustly modeling complex inter-component relationships. However, this configuration also presents significant challenges due to the intractability of the partition functions \mathcal{Z}_p and \mathcal{Z}_q , which are critical to the prior and posterior distributions. The ELBO for this model configuration is as follows:

$$\begin{aligned} \text{ELBO} = & \mathbb{E}_{q_\phi(\mathbf{z}|\mathbf{X})} [p(X|z)] - \log \left(\frac{\mathcal{Z}_p}{\mathcal{Z}_q} \right) \\ & - \mathbb{E}_{q_\phi(\mathbf{z}|\mathbf{X})} \left[\sum_{i < j} (\psi_{i,j}^p(z_i, z_j) - \psi_{i,j}^q(z_i, z_j)) \right] \\ & - \mathbb{E}_{q_\phi(\mathbf{z}|\mathbf{X})} \left[\sum_i (\psi_i^p(z_i) - \psi_i^q(z_i)) \right] \end{aligned} \quad (18)$$

While direct computation of \mathcal{Z}_p and \mathcal{Z}_q remains elusive, we can effectively estimate the gradient of the log partition function with respect to the model parameters (θ) through sampling. This estimation can be expressed as follows [30]:

$$\nabla_\theta \ln \mathcal{Z}_\theta = \nabla_\theta \ln \sum_{\mathbf{z}} \exp(-E_\theta(\mathbf{z})) = -\mathbb{E}_{p_\theta(\mathbf{z})} [\nabla_\theta E_\theta(\mathbf{z})] \quad (19)$$

Component	Layer	Units	Activation
Encoder	Fully Connected	2×256	ReLU
	Fully Connected	256×256	ReLU
	Fully Connected - σ_{shared}	$256 \times latent$	Linear
	Fully Connected - $logvar_{shared}$	$256 \times latent$	Linear
	(if factorized) Fully Connected - $\sigma_{specific}$	$256 \times latent$	Linear
Decoder	(if factorized) Fully Connected - $logvar_{specific}$	$256 \times latent$	Linear
	Fully Connected	$input \times 256$	ReLU
	Fully Connected	256×256	ReLU
	Fully Connected	256×2	Linear

TABLE IV
ARCHITECTURE DETAILS OF THE ENCODERS AND DECODERS USED IN THE COPULA EXPERIMENT.

Layer	Input Channels	Output Channels	Kernel Size	Stride	Note
Conv2d (conv_0)	fin	$fhidden$	3×3	1	Padding=1
Activation	–	–	–	–	LeakyReLU (0.2)
Conv2d (conv_1)	$fhidden$	$fout$	3×3	1	Padding=1, bias enabled
Activation	–	–	–	–	LeakyReLU (0.2)
Shortcut (if $fin \neq fout$)	fin	$fout$	1×1	1	Learned (no padding)

TABLE V
RESNET BLOCK ARCHITECTURE. EACH BLOCK CONSISTS OF TWO CONVOLUTIONAL LAYERS WITH LEAKYRELU ACTIVATIONS AND AN OPTIONAL LEARNED SHORTCUT WHEN THE INPUT AND OUTPUT CHANNEL DIMENSIONS DIFFER.

Stage	Layer Type	Output Dimensions	Activation
Input	Image	Input size	–
Initial Conv	Conv2d (3 \rightarrow 32, kernel=3, padding=1)	Input size	–
ResNet Blocks	Sequence of ResNet blocks with AvgPool (3 blocks)	$nf_0 \times s_0 \times s_0$	LeakyReLU (0.2)
Flatten	View into vector	$nf_0 \cdot s_0^2$	–
FC Layers mod	Two separate fully-connected layers	Latent Dimension	–
FC Layers joint	Two separate fully-connected layers	Latent Dimension	–
FC Layer off-diag	One fully-connected layer	Latent Dimension	–

TABLE VI
ENCODER ARCHITECTURE FOR POLYMNIST AND BIKED. THE ENCODER FIRST APPLIES A CONVOLUTION TO THE INPUT IMAGE, FOLLOWED BY A SERIES OF RESNET BLOCKS WITH AVERAGE POOLING. THE FINAL FEATURE MAP IS FLATTENED AND PROCESSED BY FULLY-CONNECTED LAYERS TO GENERATE THE LATENT MEAN AND DIAGONAL COVARIANCE PARAMETERS. FOR ALL BASELINE MODELS EXCEPT OURS, THE "FC LAYERS MOD" AND "FC LAYERS JOINT" CORRESPOND TO THE MODALITY-SPECIFIC AND SHARED POSTERIOR ENCODINGS, RESPECTIVELY. IN CONTRAST, OUR ARCHITECTURE USES AN ADDITIONAL FULLY CONNECTED LAYER "FC LAYER OFF-DIAG" TO ENCODE THE EMBEDDING UTILIZED BY THE GLOBAL ENCODER FOR GENERATING THE OFF-DIAGONAL ELEMENTS OF THE COVARIANCE MATRIX.

Stage	Layer Type	Output Dimensions	Activation
Input	Latent vector	Latent Dimension (*2 for all models but ours)	–
FC Layer	Fully-connected	$nf_0 \times s_0 \times s_0$	–
Reshape	Reshape to tensor	$256 \times 8 \times 8$	–
Upsampling	Sequential ResNet blocks with Upsample (scale factor=2)	Gradually upsample to $nf \times 64 \times 64$	LeakyReLU (0.2)
Output Conv	Conv2d (from nf to 3 channels, kernel=3, padding=1)	Output size	–

TABLE VII
DECODER ARCHITECTURE FOR POLYMNIST. THE DECODER MAPS A LATENT VECTOR TO A FEATURE MAP VIA A FULLY-CONNECTED LAYER, FOLLOWED BY A SEQUENCE OF RESNET BLOCKS WITH UPSAMPLING TO RECONSTRUCT THE IMAGE.

where $E_\theta(\mathbf{z}) = \sum_{i < j} \psi_{i,j}(z_i, z_j) + \sum_i \psi_i(z_i)$ represents the energy of configuration \mathbf{z} under the model parameters θ . This approach enables us to navigate the partition function's intractability, facilitating the model's training through gradient-based optimization techniques.

Parameter	PolyMNIST	BIKED
Encoder		
s_0	7	8
nf	64	32
nf_{\max}	1024	512
Image Size	28×28	64×64
Decoder		
s_0	7	8
nf	64	32
nf_{\max}	512	256
Output Size	28×28	64×64

TABLE VIII

SUMMARY OF THE GMRF MCVAE ARCHITECTURE. FOR POLYMNIST, THE ENCODER USES $s_0 = 7$, $nf = 64$, AND $nf_{\max} = 1024$ WITH INPUT IMAGES OF SIZE 28×28 , WHILE THE DECODER USES $s_0 = 7$, $nf = 64$, AND $nf_{\max} = 512$. FOR BIKED, THE ENCODER IS CONFIGURED WITH $s_0 = 8$, $nf = 32$, AND $nf_{\max} = 512$ (INPUT SIZE 64×64), AND THE DECODER WITH $s_0 = 8$, $nf = 32$, AND $nf_{\max} = 256$. NOTE THAT OUR GMRF MCVAE EMPLOYS A SINGLE LATENT SPACE AUGMENTED WITH AN ADDITIONAL FULLY-CONNECTED LAYER FOR OFF-DIAGONAL EMBEDDINGS, IN CONTRAST TO BASELINE MODELS THAT REQUIRE SEPARATE LATENT SPACES FOR JOINT AND MODALITY-SPECIFIC REPRESENTATIONS.

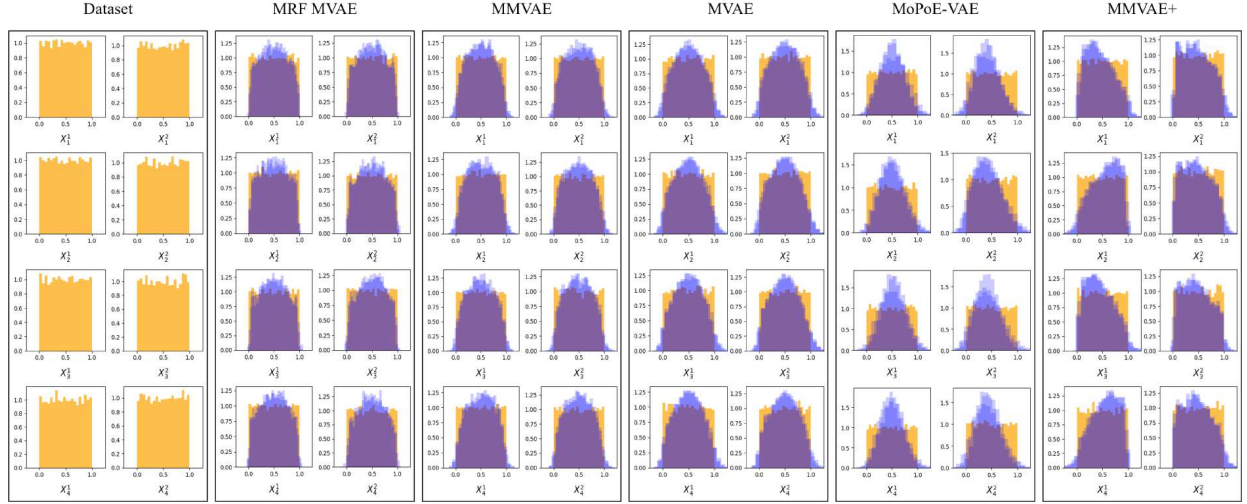


Fig. 5. Qualitative analysis of unconditional generations using the Copula dataset. Each subplot displays the marginal distributions for each coordinate: (\mathbf{x}_i^1) on the left and (\mathbf{x}_i^2) on the right, across four two-dimensional components $(\mathbf{x}_1, \mathbf{x}_2, \mathbf{x}_3, \mathbf{x}_4)$. True distributions are depicted in orange and generated distributions in blue.

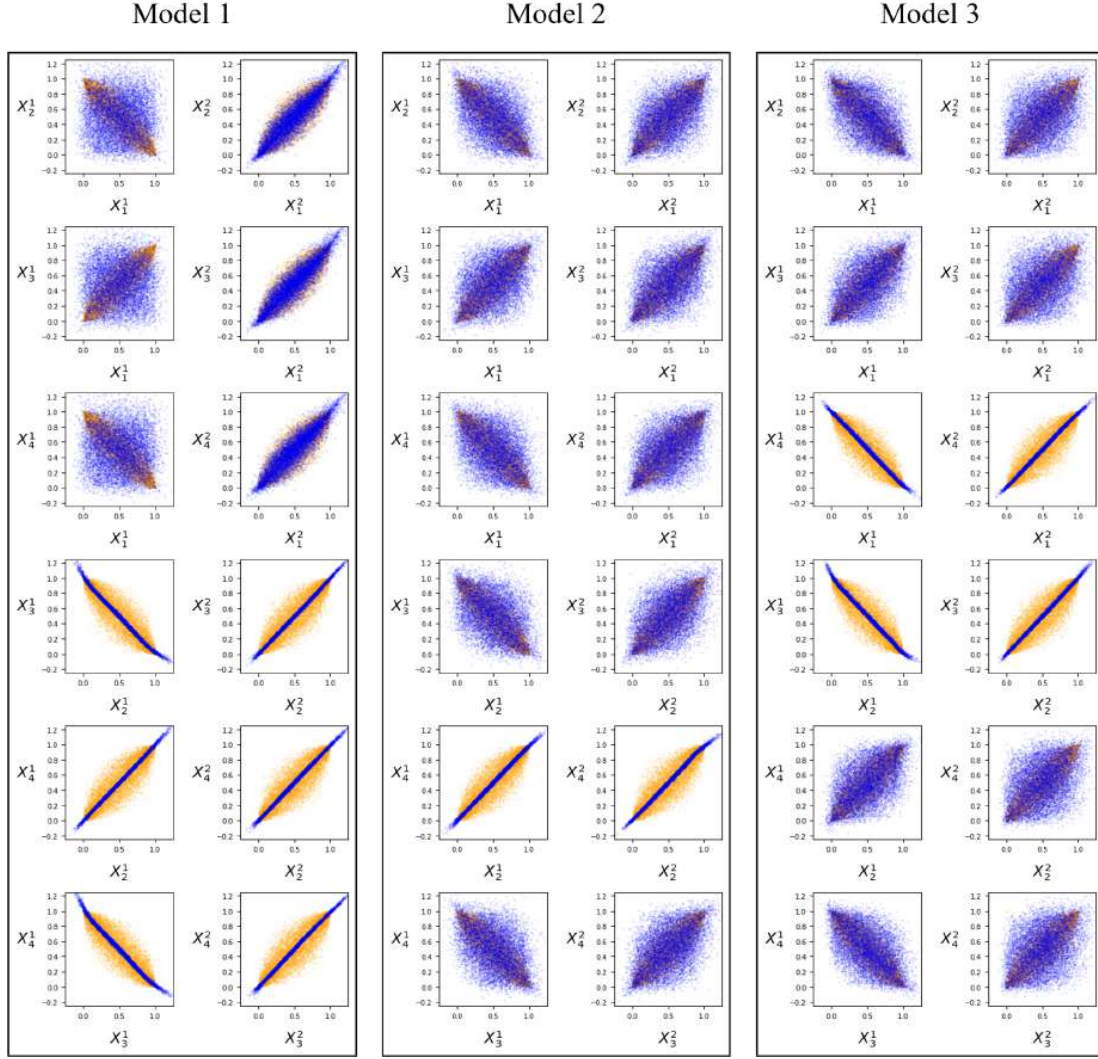


Fig. 6. Qualitative results of unconditional generations from the Copula dataset across three training iterations of the MVAE. Each subplot shows joint distributions for pairs of coordinates (x_i^1, x_j^1) and (x_i^2, x_j^2) across the four two-dimensional components (x_1, x_2, x_3, x_4) . The true distributions are shown in orange, and the MVAE-generated distributions are in blue.